Frontiers in Bioscience Landmark

Front. Biosci. (Landmark Ed) **2026**; 31(2): 48325
https://doi.org/10.31083/FBL48325

Original Research

Ferroptosis Induction by Purple Sweet Potato Anthocyanins in T-cell Acute Lymphoblastic Leukemia: Combined Molecular Docking, *In Vitro*, and *In Vivo* Evidence

Yan Zeng[1,2,†], Lanqin Liu[1,†], Jing Liu[1], Qulian Guo[1], Kaixuan Zeng[1], Yangchun Liu[1], Yongqi Bai[1], Yanling Jin[3], Xiaoli Zheng[2], Wenjun Liu[1,*], Ling Guo[1,*]

[1]Department of Pediatric Hematologic Oncology and Respiratory, Children's Medical Center, The Affiliated Hospital of Southwest Medical University, Sichuan Clinical Research Center for Birth Defects, Southwest Medical University, 646000 Luzhou, Sichuan, China
[2]Basic Medical School, Southwest Medical University, 646000 Luzhou, Sichuan, China
[3]Agricultural Microbial Agents Key Laboratory of Sichuan Province, National Engineering and Research Center for Natural Medicines, Chengdu Institute of Biology, Chinese Academy of Sciences, 610213 Chengdu, Sichuan, China
*Correspondence: wenjun_liu@swmu.edu.cn (Wenjun Liu); guoling@swmu.edu.cn (Ling Guo)
†These authors contributed equally.

Academic Editors: Kota V. Ramana and Christian Borgo
Submitted: 17 November 2025 Revised: 30 December 2025 Accepted: 8 January 2026 Published: 31 January 2026

Abstract

Background: Purple sweet potato anthocyanins (PSPAs), a class of dietary flavonoids, have shown anticancer potential. However, their ability to induce ferroptosis in T-cell acute lymphoblastic leukemia (T-ALL) remains unexplored. This study aimed to investigate whether PSPAs can trigger ferroptosis in T-ALL cells and to elucidate the underlying mechanisms. **Methods**: Jurkat T-ALL cells were treated with PSPAs, and cell viability, reactive oxygen species (ROS), lipid peroxidation, intracellular Fe^{2+}, and expression of ferroptosis-related proteins (glutathione peroxidase 4 (GPX4), solute carrier family 7 member 11 (SLC7A11), nuclear factor erythroid 2-related factor 2 (Nrf2)) were assessed. Ferrostatin-1 was used to verify ferroptosis involvement. Ultrastructural changes were examined by electron microscopy. Molecular docking was performed to evaluate PSPA binding to SLC7A11, and *in vivo* efficacy was tested in T-ALL xenograft mice. **Results**: PSPAs exhibited significant cytotoxicity in Jurkat cells, which was reversed by ferrostatin-1, indicating ferroptosis involvement. Treatment elevated ROS and lipid peroxidation, increased intracellular Fe^{2+}, and downregulated GPX4 and SLC7A11 without altering Nrf2, suggesting that SLC7A11 may be directly targeted. Electron microscopy revealed hallmark ferroptotic changes, including increased mitochondrial membrane density, loss of cristae, and rupture of the outer membrane. Molecular docking demonstrated strong binding of four PSPA components to multiple residues of SLC7A11, including Cys158, a key functional site. *In vivo*, PSPAs markedly inhibited tumor growth in T-ALL xenograft mice, achieving up to 75% suppression, as evidenced by histological analysis showing disrupted tumor architecture and cell membrane rupture. **Conclusions**: This study provides the first evidence that PSPAs induce ferroptosis in T-ALL through modulation of the SLC7A11/GPX4 pathway. These findings reveal new mechanistic insights into ferroptosis in T-ALL and highlight PSPAs as safe, naturally derived therapeutic agents with promising therapeutic potential for leukemia.

Keywords: anthocyanins; leukemia; ferroptosis; amino acid transport system Xc–; glutathione peroxidase 4

1. Introduction

Acute lymphoblastic leukemia (ALL) is a malignant hematologic disorder arising from the clonal proliferation of immature B or T lymphoid precursors. Advances in targeted agents and optimized chemotherapy regimens have markedly improved outcomes in B-cell acute lymphoblastic leukemia (B-ALL), with 5-year event-free survival (EFS) rates exceeding 85% and overall survival (OS) rates surpassing 90%. In contrast, therapeutic outcomes for T-cell acute lymphoblastic leukemia (T-ALL) remain inferior by approximately 5–10% [1]. T-ALL generally exhibits greater resistance to conventional chemotherapeutics compared with B-ALL. Although chimeric antigen receptor T-cell (CAR-T) therapy has shown applicability in T-ALL, its clinical use is hindered by challenges such as fratricide among CAR-T cells and the complexity of the T-ALL immune microenvironment [2]. The lack of effective novel agents, coupled with the toxic side effects and multidrug resistance associated with current chemotherapeutics, continues to limit treatment success in T-ALL. This situation underscores the urgent need to develop new therapeutic strategies with improved efficacy and reduced toxicity, including natural small-molecule compounds.

Flavonoids, a diverse class of naturally occurring polyphenolic compounds, have been shown to inhibit tumor cell proliferation and migration in various malignancies, including breast and thyroid cancers [3,4], and are increasingly recognized as potential adjuvants to conventional chemotherapy [5]. Epidemiological evidence suggests that

dietary flavonoid intake is inversely associated with cancer mortality [6]. Purple sweet potato anthocyanins (PSPAs), a subclass of flavonoids derived from tuber crops, exhibit higher content and greater stability than anthocyanins from grapes or black soybeans [7,8]. Their safety profile is well established, as they are sourced from a widely consumed food. Previous studies by Guo *et al*. [9,10] demonstrated that PSPAs can induce apoptosis and cell-cycle arrest in leukemia cells. However, whether PSPAs can trigger ferroptosis in cancer cells has not been investigated. Most studies on PSPAs have focused on classical forms of cell death, whereas growing evidence indicates that certain flavonoids can modulate ferroptosis in cancer cells, such as Typhaneoside in acute myeloid leukemia [11], and Quercetin in hepatocellular carcinoma [12]. These findings raise the possibility that PSPAs may also induce ferroptosis in malignant cells.

Ferroptosis is an iron-dependent, regulated form of cell death [13] characterized by excessive lipid peroxidation, elevated reactive oxygen species (ROS) generation, and intracellular Fe^{2+} accumulation [14]. Mechanistically, suppression of solute carrier family 7 member 11 (SLC7A11) impairs the activity of glutathione peroxidase 4 (GPX4), leading to lipid peroxide accumulation and the initiation of ferroptosis [15]. Conversely, SLC7A11 overexpression can inhibit ferroptosis, decrease drug sensitivity, and promote tumor proliferation and metastasis in glioblastoma [16], ovarian cancer [17], lung cancer [18] and gastric cancer [19]. Accordingly, SLC7A11 is recognized as a critical regulator of ferroptosis and is considered both a prognostic biomarker and a potential therapeutic target in cancer [20,21].

T-ALL cells exhibit metabolic characteristics of high reactive oxygen species levels and elevated iron demand. In our previous study, we demonstrated that PSPAs induce ROS production and apoptosis in T-ALL cells *in vitro* [10]. As a natural compound, PSPAs can induce reactive oxygen species accumulation and inhibit GPX4 activity. Given the established link between ROS generation and ferroptosis, we hypothesized that PSPAs may also induce ferroptosis in T-ALL cells. To date, no study has examined this possibility, nor has the anti-leukemic effect of PSPAs been validated *in vivo*.

In the present study, we employed the human T-ALL cell line Jurkat and a corresponding murine model to investigate whether PSPAs induce ferroptosis in T-ALL and to elucidate the underlying molecular mechanisms. Our findings provide novel mechanistic insights into the anti-leukemic potential of PSPAs and suggest their promise as a therapeutic strategy for T-ALL.

2. Materials and Methods

2.1 Regents and Chemicals

The human T-ALL cell line Jurkat was obtained from the Cell Bank of the Chinese Academy of Sciences (Shanghai, China). Human umbilical vein endothelial cells (HUVECs) and mouse fibroblast L929 cells were from ATCC (American Type Culture Collection, Manassas, VA, USA). The mouse ALL cell line L1210 was purchased from Punosa Life Science and Technology (Wuhan, China). All cell lines were validated by STR profiling and tested negative for mycoplasma. Six-week-old female BALB/c nude mice were supplied by Huafukang Biotechnology (Beijing, China). Purple sweet potato anthocyanins (PSPAs), containing 25 identified anthocyanins (Table 1), were provided by the Chengdu Institute of Biology, Chinese Academy of Sciences (Chengdu, China).

RPMI-1640, DMEM, and FBS were from commercial sources. Key reagents included Ferrostatin-1 (MedChemExpress, Monmouth Junction, NJ, USA), CCK-8 kit (APExBIO, Houston, TX, USA), FITC Annexin V Apoptosis Kit (BD Biosciences), Phen Green SK diacetate (PGSK) and C11-BODIPY 581/591 (GLPBIO, San Jose, CA, USA). Primary antibodies against FTH1(#4393), GPX4 (#59735), and SLC7A11 (#12691) were from Cell Signaling Technology, Inc. (Danvers, MA, USA), dilution: 1:1000; antibodies against TfR (sc-9099) and Nrf2 (sc-365949) were from Santa Cruz Biotechnology, Inc. (Dallas, TX, USA), dilution: 1:1000; β-actin (AF5003, dilution: 1:3000) and HRP-conjugated secondary antibodies (A0208, dilution: 1:3000) were from Beyotime (Shanghai, China).

2.2 Cell Culture

T-ALL cell line Jurkat and the mouse fibroblast L929 cells were cultured in RPMI Medium 1640 with 10% FBS, 1% penicillin and streptomycin. Human Umbilical Vein Endothelial Cells (HUVECs) were cultured in DMEM supplemented with 10% FBS and 1% penicillin/streptomycin in a humid environment. Murine ALL cell line L1210 was cultured in DMEM with 10% FBS, 1% penicillin and streptomycin. These cells were incubated at 37 °C in a humidified atmosphere of 5% CO_2 and 95% air.

2.3 Cell Viability Assay

Cell viability was assessed using the CCK-8 kit [22]. Jurkat cells in the logarithmic growth phase were seeded into 96-well plates at 2×10^5 cells/mL (90 µL/well) and treated with PSPAs (0, 10, 20, 40, 60, or 80 µg/mL) for 24, 48, or 72 h. HUVECs and L929 cells were seeded at 4×10^4 cells/mL (90 µL/well) and, after 24 h of culture, exposed to PSPAs at the same concentrations for an additional 24 h. All cultures were maintained at 37 °C in a humidified atmosphere with 5% CO_2. Subsequently, 10 µL of CCK-8 solution was added to each well and incubated for 4 h, after which absorbance at 450 nm was measured using a microplate reader (Multiskan Sky, Thermo Scientific, MA, USA). Cell viability (CV) was calculated using the standard formula:

$$CV\ (\%) = (OD_{Treatment} - OD_{Blank}) / (OD_{Control} - OD_{Blank}) \times 100\%$$

Table 1. Identification of 25 anthocyanins in purple sweet potato.

Peak	(m/z)		Compounds
	M^+	Major fragment ion	
1	773	611,449,287	Cyanidin 3-sophoroside-5-glucoside
2	787	625,463,301	Peonidin 3-sophoroside-5-glucoside
3	757	595,433,271	Pelargonidin 3-sophoroside-5-glucoside
4	893	731,449,287	Cyanidin 3-p-hydroxybenzoyl sophoroside-5-glucoside
5	907	745,463,301	Peonidin 3-p-hydroxybenzoyl sophoroside-5-glucoside
6	935	773,449,287	Cyanidin 3-(6-caffeoyl sophoroside)-5-glucoside
7	949	787,463,301	Peonidin 3-caffeoyl sophoroside-5-glucoside
8	949	787,449,287	Cyanidin 3-(6-feruloyl sophoroside)-5-glucoside
9	963	801,463,301	Peonidin 3-(6-feruloyl sophoroside)-5-glucoside
10	933	771,433,271	Pelargonidin 3-feruloyl sophoroside-5-glucoside
11	919	757,449,287	Cyanidin 3-(6-coumaryl sophoroside)-5-glucoside
12	933	771,463,301	Peonidin 3-(6-coumaryl sophoroside)-5-glucoside
13	1097	935,449,287	Cyanidin 3-(6″,6‴-dicaffeoyl sophoroside)-5-glucoside
14	1111	949,463,301	Peonidin 3-(6″,6‴-dicaffeoyl sophoroside)-5-glucoside
15	1055	893,449,287	Cyanidin 3-caffeoyl-p-hydroxybenzoyl sophoroside-5-glucoside
16	1069	907,463,301	Peonidin 3-caffeoyl-p-hydroxybenzoyl sophoroside-5-glucoside
17	1111	949,449,287	Cyanidin 3-(6-caffeoyl-6-feruloyl sophoroside)-5-glucoside
18	1125	963,463,301	Peonidin 3-(6-caffeoyl-6-feruloyl sophoroside)-5-glucoside
19	1127	965,463,301	Peonidin 3-feruloyl-p-caffeoyl sophoroside-5-glucoside
20	1109	947,463,301	Peonidin 3-feruloyl-p-coumaryl sophoroside-5-glucoside
21	1125	963,449,287	Cyanidin 3-(6″,6‴-diferuloyl sophoroside)-5-glucoside
22	1139	977,463,301	Peonidin 3-(6″,6‴-diferuloyl sophoroside)-5-glucoside
23	1095	933,463,301	Peonidin 3-caffeoyl-p-coumaryl sophoroside-5-glucoside
24	1069	907,449,287	Cyanidin 3-feruloyl-p-hydroxybenzoyl sophoroside-5-glucoside
25	1083	921,463,301	Peonidin 3-feruloyl-p-hydroxybenzoyl sophoroside-5-glucoside

2.4 Apoptosis Assay

Based on the IC_{50} value, Jurkat cells were seeded in six-well plates at 6×10^5 cells/mL and treated with PSPAs (0, 10, 20, or 40 µg/mL) for 24 h. For combination treatment, cells were pre-incubated with 10 µM Ferrostatin-1 (Fer-1) for 2 h before PSPA exposure. Apoptosis was assessed using the FITC Annexin V/PI kit according to the manufacturer's protocol [9]. Briefly, cells were stained in the dark for 15 min, mixed with binding buffer (Procell, Wuhan, China), and analyzed by flow cytometry (BD FACSVerse, San Diego, CA, USA) using CellQuest (BD) and FACSuite software.

2.5 Measurement of ROS

Intracellular ROS levels were measured using the fluorescent probe DCFH-DA (10 µM) for 40 min in the dark [23]. Jurkat cells treated with different concentrations of PSPAs were assessed for ROS fluorescence intensity and distribution by fluorescence microscopy, and quantitatively analyzed by flow cytometry.

2.6 Lipid Peroxidation Sensors C11 BODIPY 581/591

Lipid peroxidation was assessed using the C11-BODIPY 581/591 probe according to the manufacturer's instructions. Jurkat cells treated with different concentrations of PSPAs were analyzed by flow cytometry to quantify lipid peroxidation levels.

2.7 PGSK Detection

Intracellular Fe^{2+} levels were measured using the PGSK probe following the manufacturer's instructions. Jurkat cells treated with different concentrations of PSPAs were analyzed by flow cytometry to assess changes in Fe^{2+} content.

2.8 Cell and Organelle Morphological Changes

Following fixation, dehydration, infiltration, embedding, polymerization, and staining, ultrastructural changes in cells and organelles were examined by transmission electron microscopy (JEOL, Osaka, Japan) in the 20 µg/mL PSPA-treated and control groups.

2.9 Western Blot Analysis

Western blotting was performed as previously described. Briefly, treated cells were collected, washed with PBS, and lysed in precooled Radio-Immunoprecipitation Assay (RIPA) lysis buffer containing protease and phosphatase inhibitors (Hoffmann-La Roche, Basel, Switzerland). Lysates were centrifuged, and protein concentrations were determined by the Bradford assay using bovine

serum albumin as the standard. Equal amounts of protein (30 µg) were resolved by SDS-PAGE and transferred onto PVDF membranes. Membranes were incubated with primary antibodies at 4 °C for 12 h and with HRP-conjugated secondary antibodies at room temperature for 1 h. Protein bands were visualized using a chemiluminescence system (Beijing Si'an Biotechnology, Beijing, China) and quantified with ImageJ software (version 1.53a, NIH, Bethesda, MD, USA).

2.10 Molecular Docking

The 3D structure of PSPAs was retrieved from the PubChem database (https://pubchem.ncbi.nlm.nih.gov), and the SLC7A11 protein structure (PDB ID: 7CCS) was obtained from the RCSB PDB database (https://www.rcsb.org). Molecular docking was performed following the method of using KingDraw (Qingdao KingAgroot Precision Agriculture Technology Co., Ltd., Qingdao, Shandong, China, http://www.kingdraw.cn/), AutoDock 4 (https://autodock.scripps.edu/), and PyMOL3.0.3 (Schrödinger, Inc., https://pymol.org/). The docking conformations between small-molecule ligands and protein receptors were visualized, with potential binding sites highlighted and labeled. A binding energy of <-5 kcal/mol was considered indicative of strong binding affinity [24].

2.11 In Vivo Model Construction

The 6-week-old female nude mice were purchased from Beijing Huafukang Biological Technology Co., Ltd. Twelve female nude mice were randomly divided into control and experimental groups (n = 6 per group). Cyclophosphamide (CTX) was administered intraperitoneally for two consecutive days to induce immunosuppression. Subsequently, tumor-bearing models were established by subcutaneous injection of cell suspensions. Mice were maintained in a 12:12 h light/dark cycle and at constant temperature (24 ± 1 °C) with free access to food and water. Once tumors became palpable, the experimental group received PSPAs (75 mg/kg) by oral gavage, while the control group was gavaged with an equal volume of distilled water. Body weight and tumor size were recorded every two days. On day 12 after treatment initiation, all mice were humanely euthanized under deep isoflurane anesthesia. Animals were placed in an induction chamber (RWD R415, RWD Life Science Co., Ltd) with 5% isoflurane in 100% oxygen at least 5 minutes to ensure deep anesthesia, then cervical dislocation. Following euthanasia, tumors were excised, fixed in 4% paraformaldehyde, embedded in paraffin, sectioned at 4 µm, and processed for hematoxylin and eosin (H&E) staining for histological evaluation. All animal experiments were carried out in accordance with the recommendations of the US National Institutes of Health's Guide for the Care and Use of Laboratory Animals. This study was approved by the Ethics Committee of Southwest Medical University (Approval No. 20211019-002).

2.12 Data Analysis

Data are presented as mean ± standard deviation (SD), and statistical significance was determined using Student's *t*-test or one-way ANOVA as appropriate, with $p < 0.05$ considered statistically significant. Statistical analyses were performed using Graphpad Prism 8.3 (GraphPad Software, LLC; Boston, MA, USA). Cell viability, apoptosis assay, ROS, lipid peroxidation, PGSK and Western blotting experiments were performed with three independent replicates. The analysis results of histogram plots were generated using the CNSknowall platform (https://cnsknowall.com), a comprehensive web service for data analysis and visualization.

3. Results

3.1 PSPAs Inhibited the T-ALL Cell Proliferation

The inhibitory effect of PSPAs on the proliferation of the T-ALL cell line Jurkat was first evaluated. Jurkat cells were treated with 10, 20, 40, 60, or 80 µg/mL PSPAs for 24, 48, or 72 h. A significant, concentration-dependent reduction in cell proliferation was observed (Fig. 1A). The IC_{50} values at 24, 48, and 72 h were determined to be 24.96 ± 3.77 µg/mL, 17.21 ± 3.44 µg/mL, and 8.28 ± 2.88 µg/mL, respectively (Fig. 1B). Based on these results, a 24 h treatment duration was selected for subsequent experiments. The inhibitory activity of PSPAs toward Jurkat cells was then compared with that toward HUVEC and L929 cells. Stronger cytotoxicity against Jurkat cells was detected, with IC_{50} values of 13.88 ± 1.95 µg/mL, 47.71 ± 10.34 µg/mL, and 43.47 ± 3.51 µg/mL, respectively (Fig. 2B). Concentrations of 10, 20, and 40 µg/mL were selected for further assays, with 20 µg/mL (close to the IC_{50}) used for Ferrostatin-1 pretreatment and ultrastructural observation. Under light microscopy, PSPA-treated Jurkat cells exhibited concentration-dependent morphological changes, including reduced cell aggregation, increased debris, and features consistent with cell shrinkage and disintegration (Fig. 1C). Collectively, these results indicate that Jurkat cell viability was markedly reduced by PSPAs, suggesting their potential as a therapeutic candidate for T-ALL.

3.2 Ferrostatin-1, an Inhibitor of Ferroptosis, Attenuated PSPAs-induced Cell Death

After 24 h of treatment with increasing concentrations of PSPAs, a progressive elevation in the proportion of apoptotic Jurkat cells was detected by flow cytometry, with apoptosis rates rising from 3.83 ± 1.02% to 69.96 ± 4.23% (Fig. 3). Pretreatment with Ferrostatin-1 (10 µM) for 2 h prior to exposure to 20 µg/mL PSPAs reduced the apoptosis rate from 56.53 ± 2.50% to 32.05 ± 6.56% compared with the corresponding group without pretreatment ($p < 0.001$) (Fig. 3). Based on these findings, it was preliminarily inferred that PSPAs-induced Jurkat cell death may involve the induction of ferroptosis.

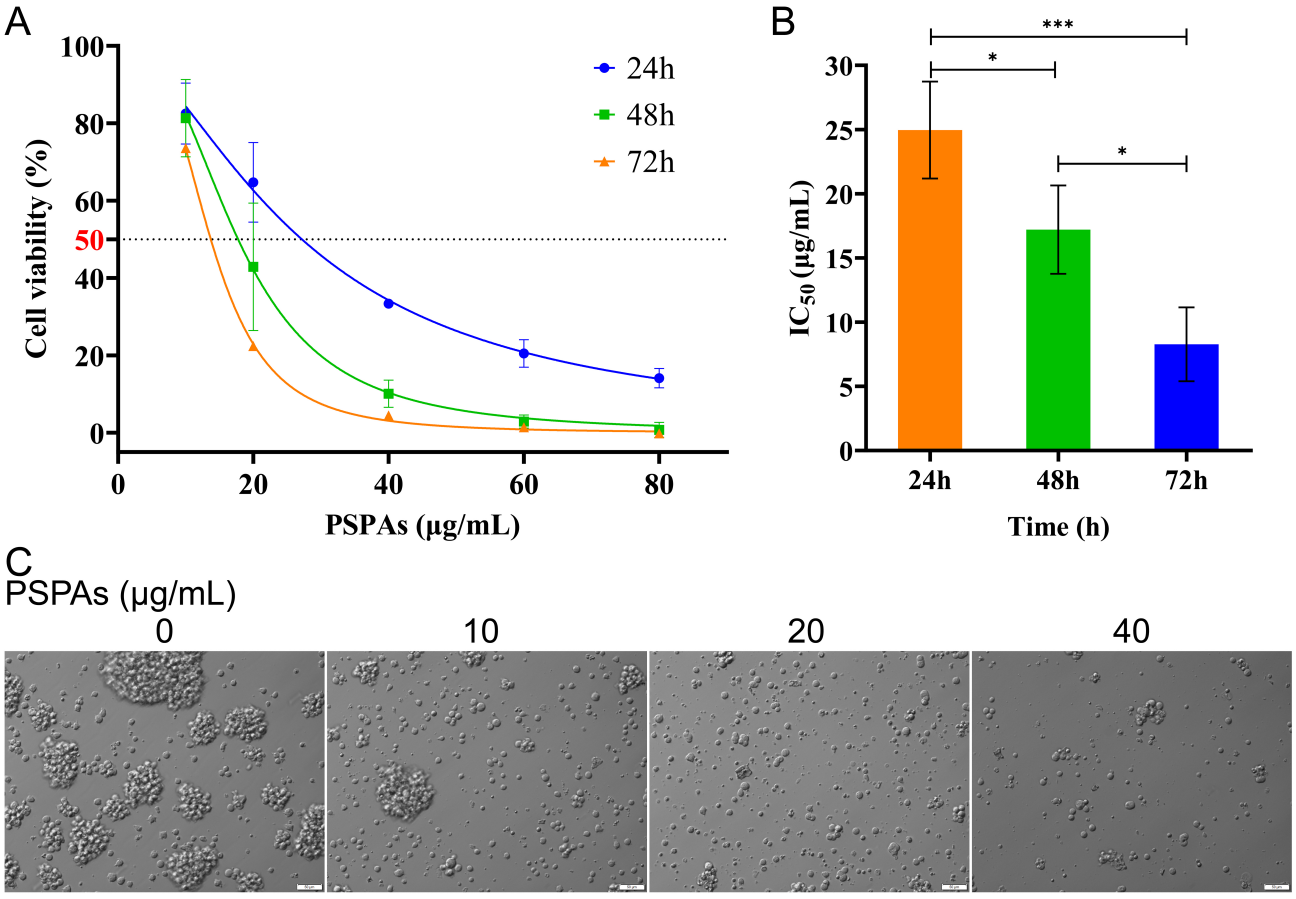

Fig. 1. Purple sweet potato anthocyanins (PSPAs) inhibited the viability of Jurkat cells (T-ALL). (A) Cell viability was measured by the CCK-8 assay after treatment with PSPAs for 24, 48, and 72 h, showing a dose-dependent inhibition. The dashed line indicates 50% cell viability, which was used as the reference threshold for IC_{50} determination. (B) IC_{50} values of PSPAs at 24, 48, and 72 h. (C) Morphological changes in Jurkat cells treated with 0, 10, 20, and 40 μg/mL PSPAs, observed under an inverted microscope (200×) (scale bar = 50 μm). Data are presented as mean ± SD (*$p < 0.05$, ***$p < 0.001$).

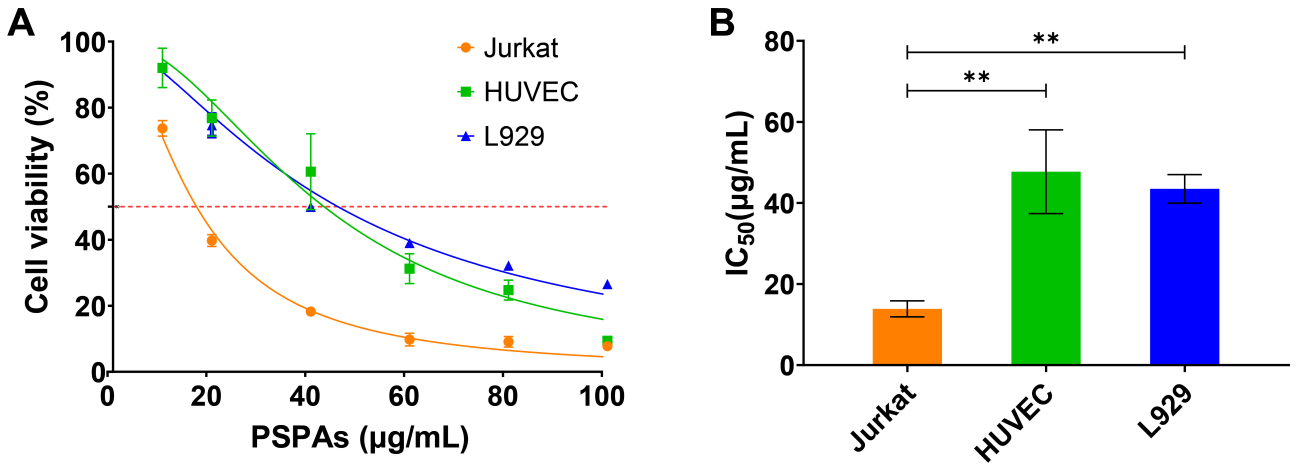

Fig. 2. Cytotoxicity of PSPAs in different cell lines. (A) Cell viability of Jurkat, Human umbilical vein endothelial cell (HUVEC), and L929 cells after 24 h PSPA treatment, assessed by the CCK-8 assay. The dashed line indicates 50% cell viability, which was used as the reference threshold for IC_{50} determination. (B) IC_{50} values of PSPAs in Jurkat, HUVEC, and L929 cells. Data are presented as mean ± SD (**$p < 0.01$).

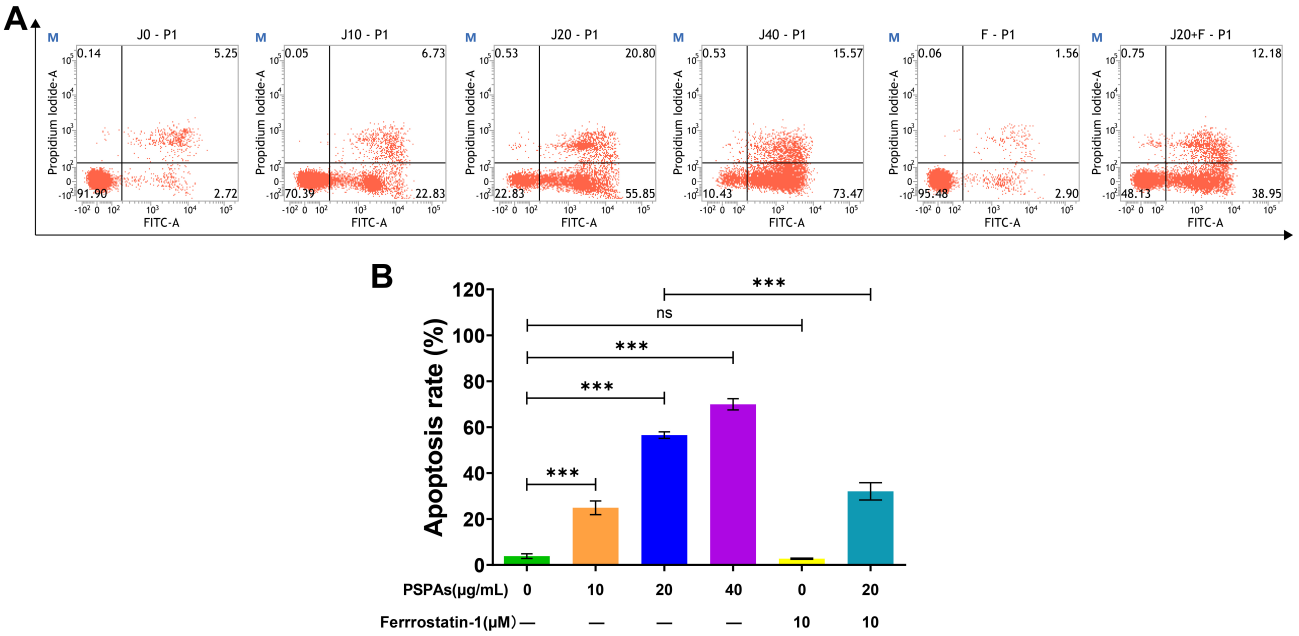

Fig. 3. Ferrostatin-1 attenuated PSPA-induced apoptosis in Jurkat cells. (A) Apoptosis rate determined by Annexin V-FITC/PI staining. (B) Statistical analysis of apoptosis rate. (ns = no significant difference, ***$p < 0.001$, -: not applicable).

3.3 PSPAs Induce Lipid Peroxidation in the T-ALL Cell

Lipid peroxidation in Jurkat cells was evaluated. As shown in Fig. 4A, ROS fluorescence intensity increased with rising PSPAs concentrations under fluorescence microscopy. This trend was further confirmed by flow cytometry (Fig. 4B,D). No significant difference in ROS levels was detected between the 10 μg/mL PSPAs group and the control; however, significant increases were observed at 20 μg/mL and 40 μg/mL (Fig. 4C). Consistently, C11-BODIPY 581/591 analysis revealed marked accumulation of lipid peroxides following PSPAs treatment (Fig. 4E), exhibiting a pattern similar to the changes in ROS. These results indicate that PSPAs induce lipid peroxidation in T-ALL cells in a concentration-dependent manner, a process considered essential for ferroptosis.

3.4 PSPAs Induced Fe^{2+} Increase in the T-ALL Cell

An increase in intracellular Fe^{2+} is recognized as another characteristic feature of ferroptosis. Flow cytometry was employed to assess PGSK green fluorescence intensity, and a significant reduction in fluorescence was observed in Jurkat cells treated with 40 μg/mL PSPAs, indicating elevated intracellular Fe^{2+} levels (Fig. 5A,B). These results demonstrate that PSPAs increase intracellular Fe^{2+} content in T-ALL cells.

3.5 Changes in the T-ALL Cell Treated With PSPAs in Electron Microscopy

In addition to alterations in cellular components, morphological changes associated with ferroptosis were examined in T-ALL cells. Transmission electron microscopy was employed to observe cellular and mitochondrial morphology. Following treatment with 20 μg/mL PSPAs, nuclei appeared slightly enlarged, irregular in shape, and displaced to one side of the cell. Compared with the control group, cell membranes were disrupted, mitochondria were reduced in size, membrane density was increased, and cristae were diminished and coarser in appearance, all features consistent with the ultrastructural characteristics of ferroptotic cells (Fig. 6). These findings visually confirmed that PSPAs induce ferroptosis in T-ALL cells.

3.6 Effect of PSPAs on Ferroptosis Related Proteins in the T-ALL Cell

The expression of FTH1 and TfR, two proteins associated with intracellular Fe^{2+} regulation, was first examined. FTH1 expression was significantly reduced after PSPAs treatment, whereas TfR expression showed no significant difference between the control and experimental groups, suggesting that FTH1 inhibition by PSPAs occurs independently of TfR (Fig. 7). We next evaluated GPX4 expression. PSPAs treatment markedly decreased GPX4 levels in Jurkat cells, resulting in the accumulation of lipid peroxides and ROS, which is consistent with earlier findings. Given that GPX4 is closely linked to SLC7A11 and Nrf2 in ferroptosis, the expression of these proteins was also assessed. PSPAs reduced SLC7A11 expression in a concentration-dependent manner, consistent with the changes observed for GPX4. In contrast, no significant alteration in Nrf2 expression was detected. Taken together, these results indicate that PSPAs induce ferroptosis in T-ALL cells primarily through inhibition of the SLC7A11/GPX4 pathway, while this process appears to be independent of TfR and Nrf2 expression.

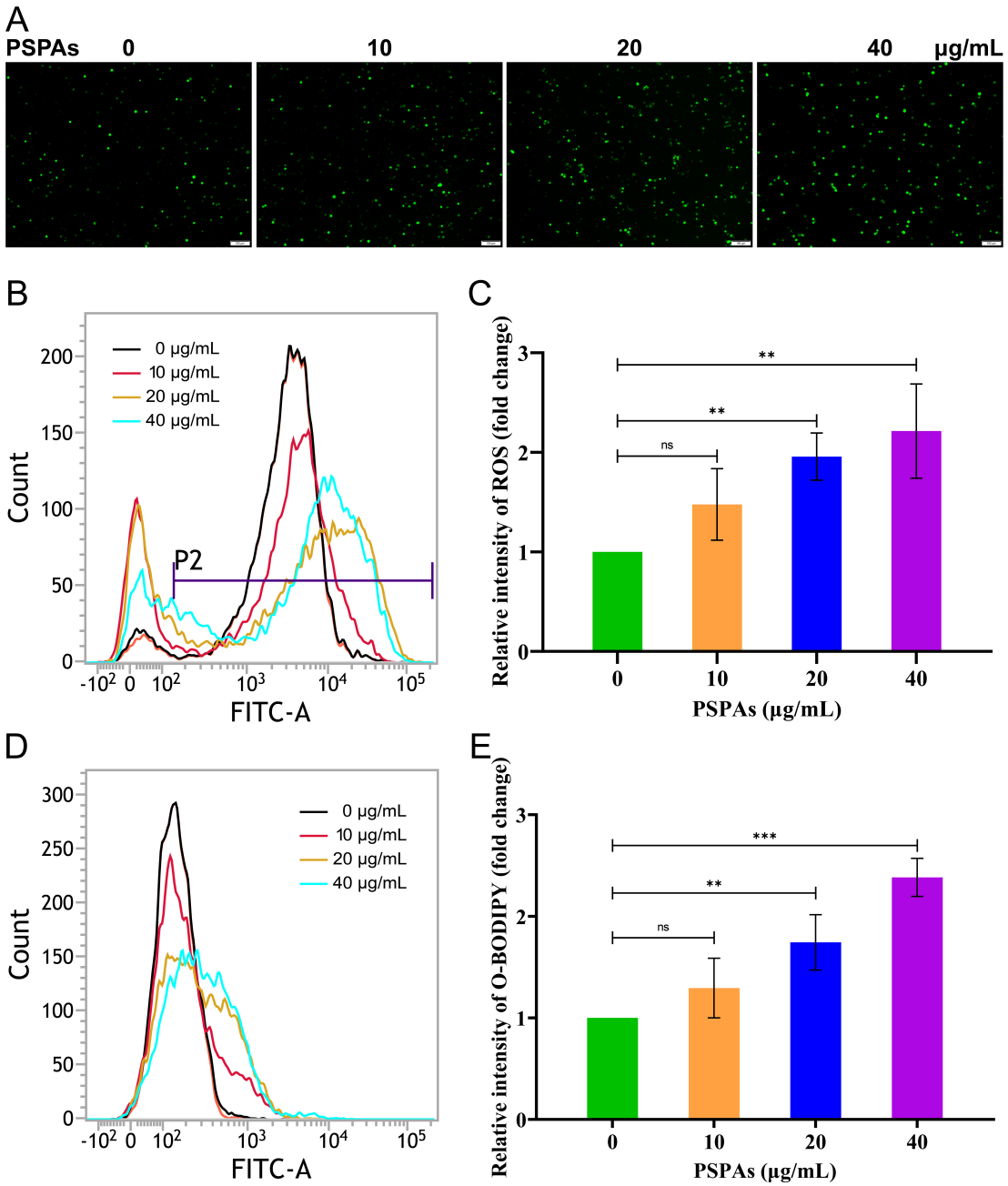

Fig. 4. PSPAs induced lipid peroxidation in Jurkat cells. (A) ROS levels in Jurkat cells treated with different concentrations of PSPAs, observed by fluorescence microscopy (scale bar = 100 μm). (B,C) ROS levels in Jurkat cells treated with different concentrations of PSPAs, analyzed by flow cytometry. P2 indicates the gate for ROS-positive cells used to evaluate intracellular ROS levels. (D,E) C11-BODIPY 581/591 detection by flow cytometry: excitation with a 488–565 nm laser, FL1 channel detection at 505–550 nm, FL2 channel detection above 580 nm; emission fluorescence shifted from 591 nm to green fluorescence around 510 nm. (**$p < 0.01$, ***$p < 0.001$, ns = no significant difference).

3.7 PSPAs can Interact With SLC7A11 Protein

Although PSPAs were shown to inhibit the SLC7A11/GPX4 pathway, the mechanism by which PSPAs regulate SLC7A11 remained unclear. To explore this interaction, molecular docking was performed between SLC7A11 and four major PSPA components: cyanidin 3-(6-caffeoyl sophoroside)-5-glucoside, peonidin 3-(6-caffeoyl sophoroside)-5-glucoside, cyanidin 3-sophoroside-5-glucoside, and peonidin 3-sophoroside-5-glucoside. The docking analysis revealed that all four components could form stable and tight interactions with the SLC7A11 protein (Fig. 8). These *in silico* findings suggest that SLC7A11 may serve as a direct molecular target of PSPAs. To further evaluate the binding stability

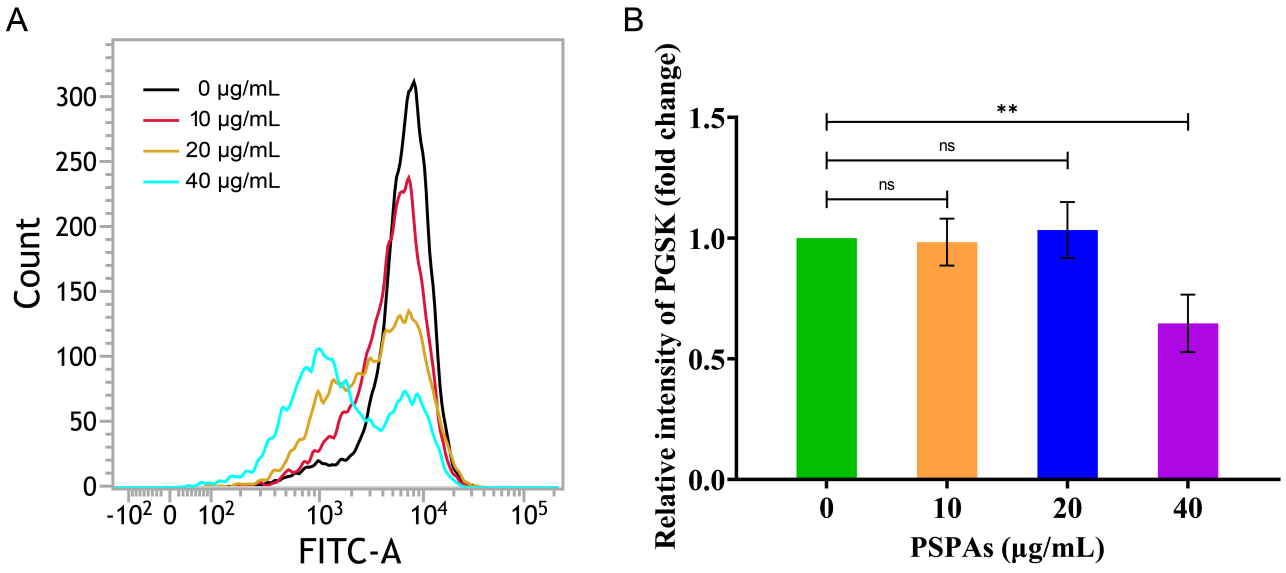

Fig. 5. PGSK levels in Jurkat cells treated with different concentrations of PSPAs, analyzed by flow cytometry. (A) PGSK fluorescence levels. (B) Statistical analysis of PGSK levels. (**$p < 0.01$, ns = no significant difference).

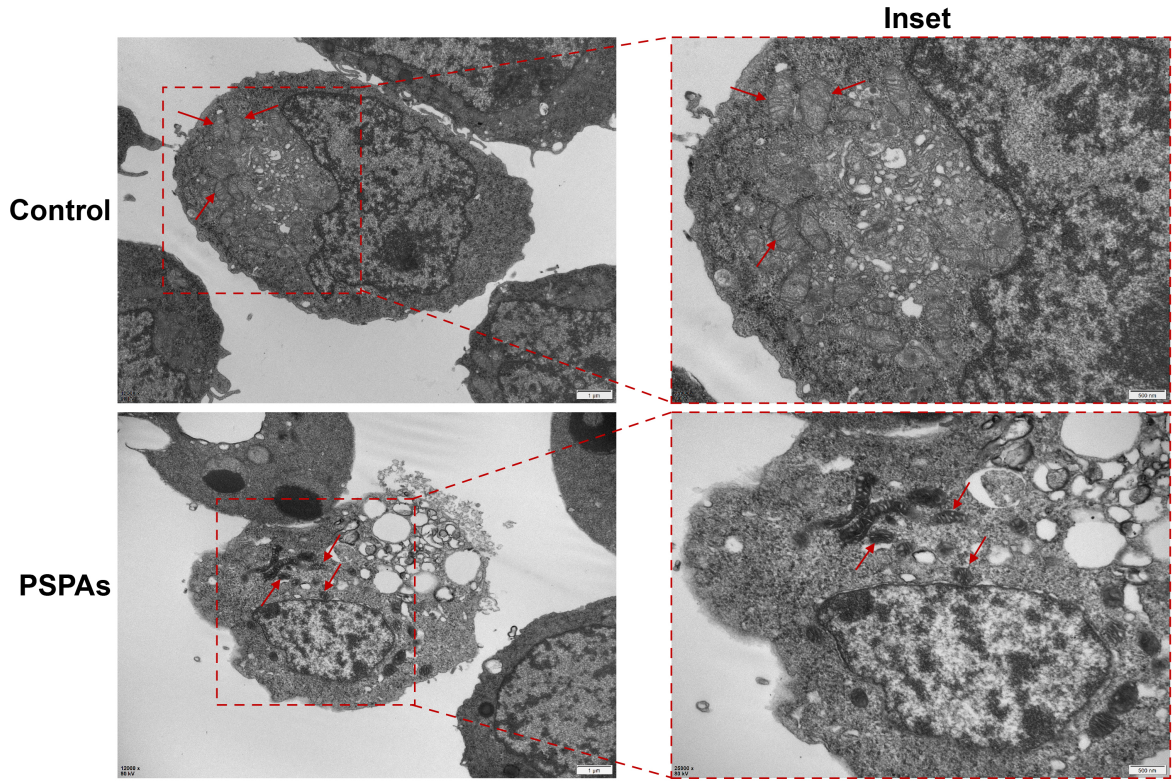

Fig. 6. Morphological changes in cells and organelles. Transmission electron microscopy (TEM) was used to observe ferroptotic features in Jurkat cells after treatment with PSPAs (20 μg/mL). Arrows indicate mitochondria (original magnification: 6000×). The left column presents low-magnification images (scale bar = 1 μm), while the right column shows the corresponding higher-magnification inset images highlighting ultrastructural details (scale bar = 500 nm).

of SLC7A11 with PSPAs, molecular dynamics simulations were performed for two representative complexes: complex 1 (cyanidin 3-sophoroside-5-glucoside–SLC7A11; binding energy = –9.5 kcal/mol) and complex 2 (cyanidin 3-(6-caffeoyl sophoroside)-5-glucoside–SLC7A11; binding energy = –8.6 kcal/mol). As shown in **Supplementary Figs. 1,2**, Complex 1 exhibited overall higher stability during the simulation, as reflected by an earlier Root Mean

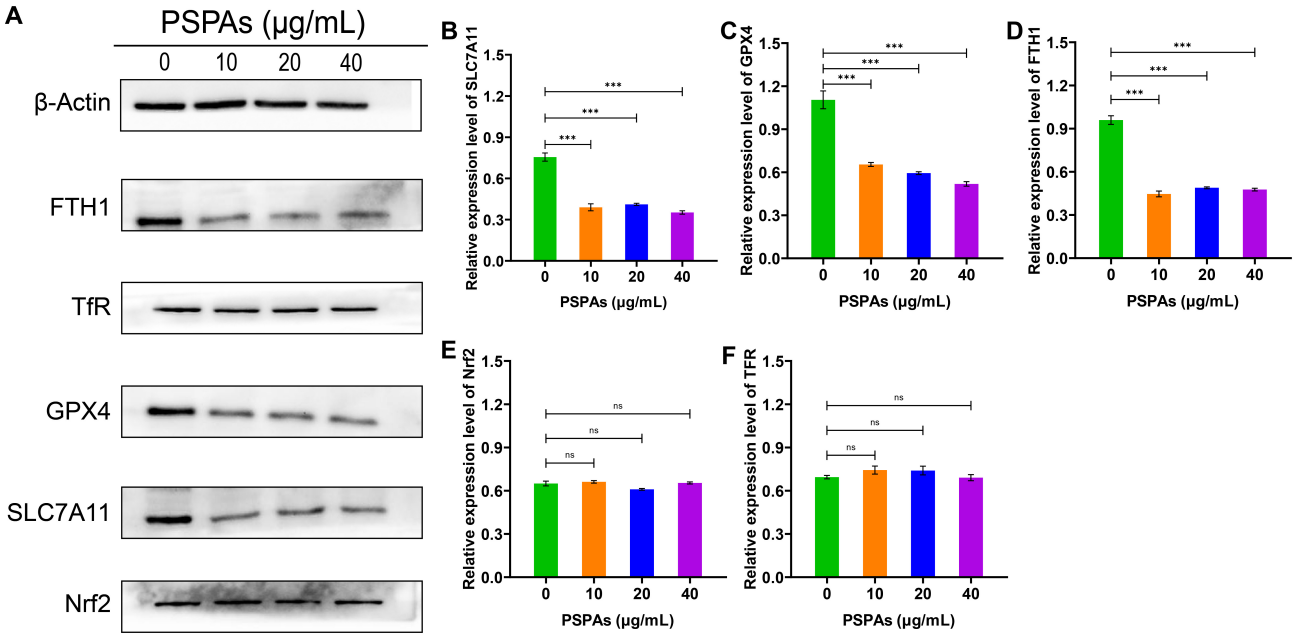

Fig. 7. Western blot analysis of ferroptosis-related proteins in Jurkat cells treated with different concentrations of PSPAs. (A) Representative Western blot images showing the protein expression levels of β-Actin, FTH1, TfR, GPX4, SLC7A11, and Nrf2 in cells treated with different concentrations of PSPAs (0, 10, 20, and 40 μg/mL). β-Actin was used as a loading control. (B–F) Quantitative analysis of the relative expression levels of SLC7A11 (B), GPX4 (C), FTH1 (D), Nrf2 (E), and TfR (F), normalized to β-Actin. Band intensities were quantified using ImageJ. (***$p < 0.001$, ns = no significant difference).

Square Deviation (RMSD) convergence with smaller fluctuations, lower residue-level flexibility, and a slight decrease in both radius of gyration and solvent-accessible surface area, whereas complex 2 showed persistent fluctuations and increased conformational heterogeneity. Although both complexes maintained comparable hydrogen bonding levels, the Gibbs free energy landscape revealed a single dominant low-energy basin for complex 1, in contrast to multiple neighboring minima for complex 2. Together, these results indicate that complex 1 adopts a more stable binding mode, and support the notion that docking-derived binding energies can serve as a reasonable indicator of relative binding affinity between PSPAs and SLC7A11.

3.8 PSPAs Have Anti-tumor Effects In Vivo

In addition to *in vitro* assays, the anti-tumor activity of PSPAs was evaluated *in vivo* using a subcutaneous xenograft model in nude mice. Tumor growth was observed over time in both the PSPA-gavaged and control groups (Fig. 9A). In the PSPA-treated group, tumor volume increased from 25.81 $\pm$ 14.38 mm^3 to 508.84 $\pm$ 179.79 mm^3, whereas in the control group it increased from 26.09 $\pm$ 7.97 mm^3 to 1294.86 $\pm$ 201.72 mm^3. Correspondingly, tumor weights were 0.53 $\pm$ 0.22 g in the PSPAs group and 2.09 $\pm$ 0.62 g in the control group, yielding an average tumor suppression rate of 75% (Fig. 9B,C). Histological examination revealed that tumor cells in the control group displayed typical leukemic morphology and active proliferation, while those in the PSPA-treated group appeared loosely arranged, reduced in density, variable in size, and exhibited disrupted cell membranes (Fig. 9D,E). Collectively, these results demonstrate that PSPAs exert significant anti-ALL effects *in vivo*.

4. Discussion

T-ALL is an aggressive hematologic malignancy characterized by poor prognosis, high early relapse rates, and a predilection for children and young adults, while being rare in older populations [25]. The event-free survival (EFS) rate remains approximately 50% in T-ALL [26], underscoring the urgent need for novel and more effective therapeutic strategies. In recent years, antioxidants derived from natural food sources have attracted considerable attention as a class of safe and potentially effective anticancer agents. Among them, flavonoids, a group of natural polyphenolic antioxidants, have been increasingly recognized not only for their free radical–scavenging properties but also for their broad antitumor activities [27]. PSPAs, rich in diverse anthocyanin compounds, represent a prominent example. Our previous studies demonstrated that PSPAs significantly inhibit the proliferation of acute lymphoblastic leukemia (ALL) cells, with 25 distinct anthocyanins identified, including cyanidin 3-(6-caffeoyl sophoroside)-5-glucoside, peonidin 3-(6-caffeoyl sophoroside)-5-glucoside, cyanidin 3-sophoroside-5-glucoside, and peonidin 3-sophoroside-5-

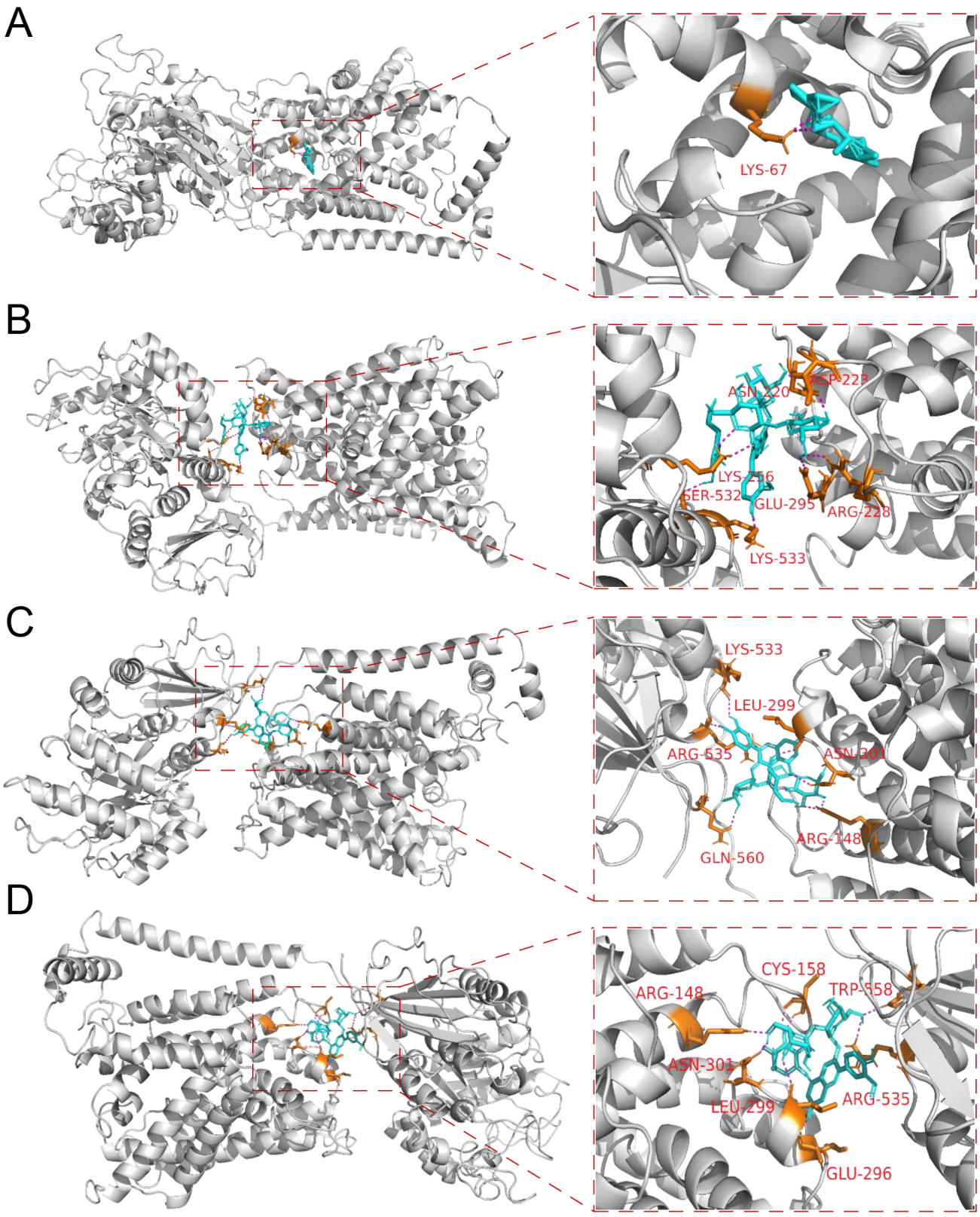

Fig. 8. Molecular docking of four PSPAs with SLC7A11 protein. (A) SLC7A11 with cyanidin 3-(6-caffeoyl sophoroside)-5-glucoside (binding energy = –8.6 kcal/mol). (B) SLC7A11 with peonidin 3-(6-caffeoyl sophoroside)-5-glucoside (binding energy = –9.1 kcal/mol). (C) SLC7A11 with cyanidin 3-sophoroside-5-glucoside (binding energy = –9.5 kcal/mol). (D) SLC7A11 with peonidin 3-sophoroside-5-glucoside (binding energy = –9.3 kcal/mol).

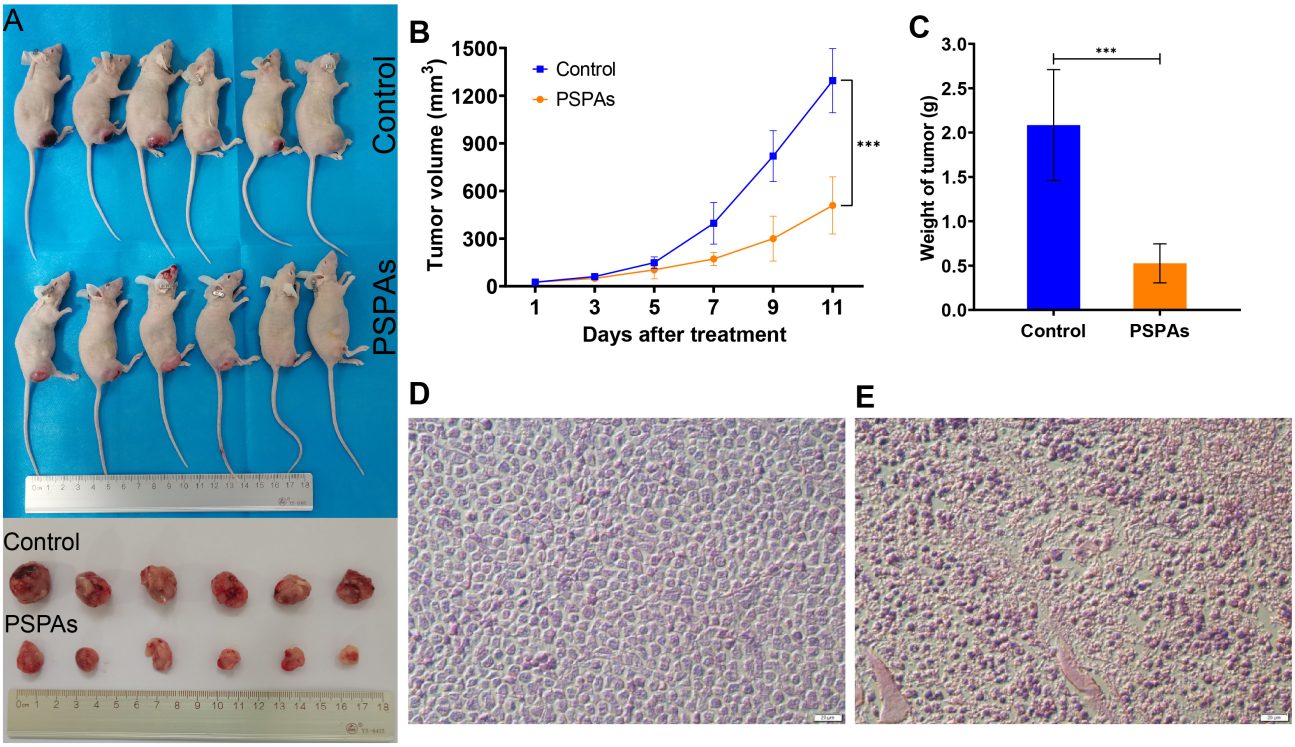

Fig. 9. *In vivo* anti-tumor effects of PSPAs. (A) Representative images showing subcutaneous tumors in the PSPAs gavage group and the control group. (B) Tumor volume changes and differences between the two groups. (C) Tumor weight differences in nude mice between the two groups. (D) Hematoxylin and eosin (H&E) staining of tumors in the control group. (E) H&E staining of tumors in the PSPAs group. Data are presented as mean ± SD (***$p < 0.001$) (scale bar = 20 μm in D and E).

glucoside as major components [10]. However, prior investigations have primarily focused on PSPA-induced apoptosis and cell-cycle arrest, with little evidence addressing their potential to trigger ferroptosis. This gap in knowledge provided the rationale for our current study, in which we investigated whether PSPAs can induce ferroptosis in T-ALL cells and explored the underlying molecular mechanisms.

In this study, PSPAs showed stronger cytotoxicity toward Jurkat T-ALL cells than toward normal HUVEC and L929 cells (Fig. 2) and promoted early cell death (Fig. 1), consistent with previous findings [9]. Notably, PSPA-induced cell death was partially reversed by the ferroptosis inhibitor Ferrostatin-1 (Fig. 3B), suggesting ferroptosis involvement.

Lipid peroxidation and Fe^{2+} accumulation are typical features of ferroptosis [14]. PSPAs increased ROS levels in Jurkat cells in a concentration-dependent manner, particularly at higher concentrations, consistent with earlier reports [28] (Fig. 4A–C). The most critical feature of ferroptosis is the peroxidation-mediated destruction of phospholipids in cellular and organelle membranes due to inactivation of the intracellular reducing system, leading to membrane rupture [29]. Consistently, lipid peroxides accumulated after PSPAs treatment, following a pattern similar to ROS changes (Fig. 4D,E). Furthermore, PGSK fluorescence was significantly reduced in the high-concentration group, indicating increased Fe^{2+} content (Fig. 5), while no obvious change was observed at lower concentrations. This may be due to the instability of Fe^{2+}, which rapidly reacts with ROS through the Fenton reaction [30].

Based on the two hallmark features of ferroptosis observed in PSPA-treated T-ALL cells, we further examined cell morphology by transmission electron microscopy. PSPAs (20 μg/mL) caused increased mitochondrial membrane density, reduced or absent cristae, and rupture of the outer membrane, while nuclei remained intact (Fig. 6). These features were consistent with ferroptosis but distinct from other forms of programmed cell death [31,32]. Combined with biochemical and ultrastructural evidence, we propose that PSPAs induce ferroptosis in T-ALL cells.

To investigate the molecular basis for lipid peroxidation and Fe^{2+} accumulation, ferroptosis-related proteins were analyzed by Western blot. FTH1 expression decreased with increasing PSPAs concentration, whereas TfR showed no significant change (Fig. 7), differing from ferroptosis induced by baicalin in bladder cancer [33]. This suggests PSPAs may directly affect FTH1. GPX4 and SLC7A11 expression was significantly reduced, while Nrf2 levels were unchanged (Fig. 7). GPX4 is the only known enzyme protecting membranes from peroxidative damage [34,35], and its loss leads to lipid peroxide accumulation and ferroptosis [36,37]. GPX4 activity depends on cystine uptake

via system Xc–, in which SLC7A11 encodes the functional xCT subunit that transports cystine in exchange for glutamate; cystine is then reduced to cysteine and used for GSH synthesis via GCL and GSS, serving as a GPX4 cofactor to reduce lipid peroxides [38,39]. Nrf2, a key regulator of SLC7A11, can downregulate SLC7A11 when reduced, thereby increasing lipid ROS and promoting ferroptosis in several cancers [40,41]. However, this was not observed here, indicating that PSPA-mediated changes in SLC7A11 and GPX4 in Jurkat cells are Nrf2-independent and may involve direct targeting of SLC7A11.

Therefore, potential binding between PSPAs and SLC7A11 was explored by molecular docking. Four major PSPA components were docked with SLC7A11, and

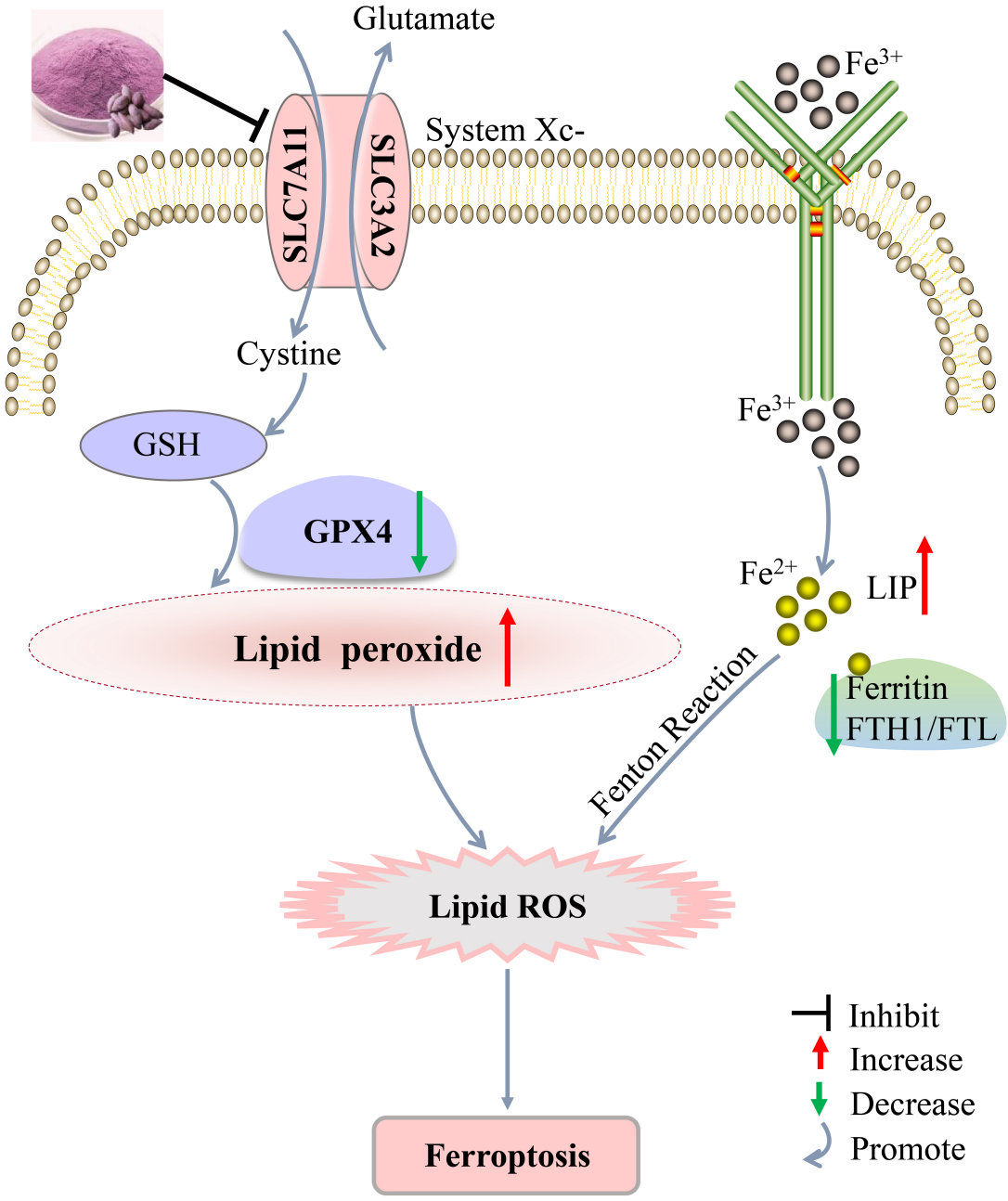

Fig. 10. Proposed mechanism by which PSPAs induce ferroptosis in T-ALL cells via the SLC7A11/GPX4 signaling pathway. system Xc–, a cystine/glutamate antiporter composed of SLC7A11 and SLC3A2, mediates cystine uptake and glutamate export. SLC7A11, solute carrier family 7 member 11; SLC3A2, solute carrier family 3 member 2; GSH, glutathione; GSSG, glutathione disulfide; R-OH, lipid alcohol; R-OOH, lipid peroxide; TfR, transferrin receptor; Ferritin, composed of the heavy chain encoded by FTH1 and the light chain encoded by FTL; LIP, labile iron pool. In the Fenton reaction, Fe^{2+} reacts with reactive oxygen species (ROS) to generate Fe^{3+} and hydroxyl radicals (·OH). ROS include hydrogen peroxide (H_2O_2), superoxide anion (O_2^-), and related species.

all showed tight binding involving 14 residues: LYS-67, LYS-266, LYS-533, SER-532, GLU-295, GLU-296, ARG-228, ARG-535, ARG-148, LEU-299, ASN-301, GLN-560, CYS-158, and TRP-558 (Fig. 8). Notably, Cys158 forms a disulfide bond with Cys211, a structural feature of System Xc [42].

Finally, the anti-leukemia effects of PSPAs were then evaluated *in vivo*. Tumor volumes increased over time in both groups, but were significantly larger in controls than in PSPA-treated mice (Fig. 9A–C). The tumor inhibition rate reached 75%. H&E staining revealed that control tumors had evenly distributed, densely arranged leukemia cells with intact structure and active growth (Fig. 9D), whereas PSPA-treated tumors were loosely arranged, reduced in volume, and showed membrane rupture (Fig. 9E). Additionally, two control mice developed lameness in the right hind limb and exhibited reduced mobility, while all PSPA-treated mice remained active. These results demonstrate that PSPAs effectively inhibit leukemia *in vivo*, representing the first report of their anti-leukemic activity in a live model.

PSPAs are water-soluble compounds that readily dissolve in aqueous environments, conferring a biological availability advantage over many poorly soluble agents. Nevertheless, their *in vivo* bioavailability and delivery efficiency warrant further investigation. Future studies will focus on optimizing delivery strategies, such as nanoencapsulation or formulation modification, to improve stability, bioavailability, and therapeutic efficacy. Importantly, PSPAs exhibit low toxicity and are considered safe for consumption due to their food origin [8]. Mechanistically, PSPAs induce oxidative stress and endoplasmic reticulum stress, leading to mitochondrial membrane potential loss, elevated ROS production, apoptosis activation, cell-cycle arrest, and disruption of calcium homeostasis, thereby exerting multi-pathway and multi-target antitumor effects [43]. Given that conventional T-ALL chemotherapeutics, including dexamethasone and cytarabine, also impose oxidative and metabolic stress on leukemia cells, PSPAs may function as complementary modulators of redox balance and ferroptosis-related signaling, providing a potential rationale for combination therapeutic strategies. Despite these findings, this study has limitations, particularly the insufficient investigation of genetic regulation of key ferroptosis modulators and their potential crosstalk with other regulated cell death pathways. Future work will employ genetic and pharmacological approaches to further elucidate ferroptosis mechanisms and their interactions with alternative cell death modes.

5. Conclusion

This study demonstrated the anti-leukemic activity of PSPAs against T-ALL both *in vitro* and, for the first time, *in vivo* in an ALL model. It also provided the first evidence that PSPAs can induce ferroptosis in Jurkat T-ALL cells, with SLC7A11 identified as a potential molecular target (Fig. 10). These findings offer new insights into the role of ferroptosis in T-ALL and highlight naturally derived, safe compounds as promising candidates for therapeutic development in this malignancy.

Availability of Data and Materials

The data that support the findings of this study are available from the corresponding author upon reasonable request.

Author Contributions

YZ performed sample collection, extraction, metabolomics analysis, and revised the final manuscript. LQL conducted part of the cell and animal experiments and wrote the main manuscript text. JL, QLG, and YQB carried out data analysis and managed experiments. KXZ and YCL performed molecular dynamics simulation. YLJ supplied the samples, data analysis and funding. XLZ designed part of the study. WJL contributed to experimental design, methodology, and funding. LG designed the study, performed molecular and cellular experiments, provided the bioinformatics platform, contributed to writing, and supported funding. All authors reviewed and approved the final manuscript. All authors contributed to editorial changes in the manuscript. All authors have participated sufficiently in the work and agreed to be accountable for all aspects of the work.

Ethics Approval and Consent to Participate

All animal experiments in this study were conducted at Southwest Medical University in strict accordance with the institutional guidelines and the Good Publication Practice in Physiology 2013 (Persson 2013). All procedures were reviewed and approved by the Ethics Committee of Southwest Medical University (Approval No.: 20211019-002).

Acknowledgment

We thank the CNSknowall platform (https://cnsknowall.com) for providing data analysis services.

Funding

This research was financially supported by Sichuan Science and Technology Program (2024YFFK0271); Sichuan Science and Technology Plan Joint Innovation Program (2022YFS0622-A3); the key project of Southwest Medical University clinical medicine special program (2025LCYXZX31, 2024LCYXZX10), National Natural Science Foundation of China (32571929) and the earmarked fund for CARS-10-Sweetpotato (CARS-10-GW24).

Conflict of Interest

The authors declare no conflict of interest.

Supplementary Material

Supplementary material associated with this article can be found, in the online version, at https://doi.org/10.31083/FBL48325.

References

[1] Reedijk AMJ, Coebergh JWW, de Groot-Kruseman HA, van der Sluis IM, Kremer LC, Karim-Kos HE, *et al*. Progress against childhood and adolescent acute lymphoblastic leukaemia in the Netherlands, 1990-2015. Leukemia. 2021; 35: 1001–1011. https://doi.org/10.1038/s41375-020-01024-0.

[2] Wei W, Yang D, Chen X, Liang D, Zou L, Zhao X. Chimeric antigen receptor T-cell therapy for T-ALL and AML. Frontiers in Oncology. 2022; 12: 967754. https://doi.org/10.3389/fonc.2022.967754.

[3] Gonçalves CFL, Hecht F, Cazarin J, Fortunato RS, Vaisman M, Carvalho DPD, *et al*. The flavonoid quercetin reduces cell migration and increases NIS and E-cadherin mRNA in the human thyroid cancer cell line BCPAP. Molecular and Cellular Endocrinology. 2021; 529: 111266. https://doi.org/10.1016/j.mce.2021.111266.

[4] Attari F, Keighobadi F, Abdollahi M, Arefian E, Lotfizadeh R, Sepehri H, *et al*. Inhibitory effect of flavonoid xanthomicrol on triple-negative breast tumor via regulation of cancer-associated microRNAs. Phytotherapy Research: PTR. 2021; 35: 1967–1982. https://doi.org/10.1002/ptr.6940.

[5] Dewanjee S, Chakraborty P, Bhattacharya H, Singh SK, Dua K, Dey A, *et al*. Recent advances in flavonoid-based nanocarriers as an emerging drug delivery approach for cancer chemotherapy. Drug Discovery Today. 2023; 28: 103409. https://doi.org/10.1016/j.drudis.2022.103409.

[6] Zhou Y, Gu K, Zhou F. Dietary Flavonoid Intake and Cancer Mortality: A Population-Based Cohort Study. Nutrients. 2023; 15: 976. https://doi.org/10.3390/nu15040976.

[7] Ryu D, Koh E. Stability assessment of anthocyanins from black soybean, grape, and purple sweet potato under in vitro gastrointestinal digestion. Food Science and Biotechnology. 2022; 31: 1053–1062. https://doi.org/10.1007/s10068-022-01071-6.

[8] Li A, Xiao R, He S, An X, He Y, Wang C, *et al*. Research Advances of Purple Sweet Potato Anthocyanins: Extraction, Identification, Stability, Bioactivity, Application, and Biotransformation. Molecules (Basel, Switzerland). 2019; 24: 3816. https://doi.org/10.3390/molecules24213816.

[9] Guo L, Jin Y, Yang Y, Liu J, Liu C, Zeng Y, *et al*. Calcicoptosis Induced by Purple Sweet Potato Anthocyanins through the Nonosmotic Regulation of the NFAT5/S100A4-S100A9 Pathway in Acute Lymphoblastic Leukemia. Chemistry & Biodiversity. 2022; 19: e202200447. https://doi.org/10.1002/cbdv.202200447.

[10] Guo L, Liu J, Yang Y, Zeng Y, Yuan F, Zhong F, *et al*. Purple sweet potato anthocyanins elicit calcium overload-induced cell death by inhibiting the calcium-binding protein S100A4 in acute lymphoblastic leukemia. Food Bioscience. 2021; 42: 101214. https://doi.org/10.1016/j.fbio.2021.101214.

[11] Zhu HY, Huang ZX, Chen GQ, Sheng F, Zheng YS. Typhaneoside prevents acute myeloid leukemia (AML) through suppressing proliferation and inducing ferroptosis associated with autophagy. Biochemical and Biophysical Research Communications. 2019; 516: 1265–1271. https://doi.org/10.1016/j.bbrc.2019.06.070.

[12] Wang ZX, Ma J, Li XY, Wu Y, Shi H, Chen Y, *et al*. Quercetin induces p53-independent cancer cell death through lysosome activation by the transcription factor EB and Reactive Oxygen Species-dependent ferroptosis. British Journal of Pharmacology. 2021; 178: 1133–1148. https://doi.org/10.1111/bph.15350.

[13] Dixon SJ, Lemberg KM, Lamprecht MR, Skouta R, Zaitsev EM, Gleason CE, *et al*. Ferroptosis: an iron-dependent form of nonapoptotic cell death. Cell. 2012; 149: 1060–1072. https://doi.org/10.1016/j.cell.2012.03.042.

[14] Chen X, Kang R, Kroemer G, Tang D. Broadening horizons: the role of ferroptosis in cancer. Nature Reviews. Clinical Oncology. 2021; 18: 280–296. https://doi.org/10.1038/s41571-020-00462-0.

[15] Koppula P, Zhuang L, Gan B. Cystine transporter SLC7A11/xCT in cancer: ferroptosis, nutrient dependency, and cancer therapy. Protein & Cell. 2021; 12: 599–620. https://doi.org/10.1007/s13238-020-00789-5.

[16] Polewski MD, Reveron-Thornton RF, Cherryholmes GA, Marinov GK, Aboody KS. SLC7A11 Overexpression in Glioblastoma Is Associated with Increased Cancer Stem Cell-Like Properties. Stem Cells and Development. 2017; 26: 1236–1246. https://doi.org/10.1089/scd.2017.0123.

[17] Hong T, Lei G, Chen X, Li H, Zhang X, Wu N, *et al*. PARP inhibition promotes ferroptosis via repressing SLC7A11 and synergizes with ferroptosis inducers in BRCA-proficient ovarian cancer. Redox Biology. 2021; 42: 101928. https://doi.org/10.1016/j.redox.2021.101928.

[18] Lin W, Wang C, Liu G, Bi C, Wang X, Zhou Q, *et al*. SLC7A11/xCT in cancer: biological functions and therapeutic implications. American Journal of Cancer Research. 2020; 10: 3106–3126.

[19] Chen L, Qiao L, Bian Y, Sun X. GDF15 knockdown promotes erastin-induced ferroptosis by decreasing SLC7A11 expression. Biochemical and Biophysical Research Communications. 2020; 526: 293–299. https://doi.org/10.1016/j.bbrc.2020.03.079.

[20] Shi ZZ, Tao H, Fan ZW, Song SJ, Bai J. Prognostic and Immunological Role of Key Genes of Ferroptosis in Pan-Cancer. Frontiers in Cell and Developmental Biology. 2021; 9: 748925. https://doi.org/10.3389/fcell.2021.748925.

[21] Zheng Z, Hong X, Huang X, Jiang X, Jiang H, Huang Y, *et al*. Comprehensive analysis of ferroptosis-related gene signatures as a potential therapeutic target for acute myeloid leukemia: A bioinformatics analysis and experimental verification. Frontiers in Oncology. 2022; 12: 930654. https://doi.org/10.3389/fonc.2022.930654.

[22] Huang Z, Shen Y, Liu W, Yang Y, Guo L, Yan Q, *et al*. Berberine targets the electron transport chain complex I and reveals the landscape of OXPHOS dependency in acute myeloid leukemia with IDH1 mutation. Chinese Journal of Natural Medicines. 2023; 21: 136–145. https://doi.org/10.1016/S1875-5364(23)60391-7.

[23] Huang Q, Ji D, Tian X, Ma L, Sun X. Berberine inhibits erastin-induced ferroptosis of mouse hippocampal neuronal cells possibly by activating the Nrf2-HO-1/GPX4 pathway. Nan Fang Yi Ke Da Xue Xue Bao. 2022; 42: 937–943. https://doi.org/10.12122/j.issn.1673-4254.2022.06.19. (In Chinese)

[24] Fang T, Liu L, Liu W. Exploring the mechanism of fraxetin against acute myeloid leukemia through cell experiments and network pharmacology. BMC Complementary Medicine and Therapies. 2024; 24: 226. https://doi.org/10.1186/s12906-024-04529-8.

[25] Liu X, Zou Y, Zhang L, Guo Y, Chen Y, Yang W, *et al*. A Novel Risk Defining System for Pediatric T-Cell Acute Lymphoblastic Leukemia From CCCG-ALL-2015 Group. Frontiers in Oncology. 2022; 12: 841179. https://doi.org/10.3389/fonc.2022.841179.

[26] Cui L, Li ZG, Chai YH, Yu J, Gao J, Zhu XF, *et al*. Outcome

of children with newly diagnosed acute lymphoblastic leukemia treated with CCLG-ALL 2008: The first nation-wide prospective multicenter study in China. American Journal of Hematology. 2018; 93: 913–920. https://doi.org/10.1002/ajh.25124.

[27] Wang M, Yu F, Zhang Y, Chang W, Zhou M. The Effects and Mechanisms of Flavonoids on Cancer Prevention and Therapy: Focus on Gut Microbiota. International Journal of Biological Sciences. 2022; 18: 1451–1475. https://doi.org/10.7150/ijbs.68170.

[28] Lou S, Hong H, Maihesuti L, Gao H, Zhu Z, Xu L, *et al*. Inhibitory effect of hydnocarpin D on T-cell acute lymphoblastic leukemia via induction of autophagy-dependent ferroptosis. Experimental Biology and Medicine (Maywood, N.J.). 2021; 246: 1541–1553. https://doi.org/10.1177/15353702211004870.

[29] Stockwell BR, Friedmann Angeli JP, Bayir H, Bush AI, Conrad M, Dixon SJ, *et al*. Ferroptosis: A Regulated Cell Death Nexus Linking Metabolism, Redox Biology, and Disease. Cell. 2017; 171: 273–285. https://doi.org/10.1016/j.cell.2017.09.021.

[30] Tang Z, Zhao P, Wang H, Liu Y, Bu W. Biomedicine Meets Fenton Chemistry. Chemical Reviews. 2021; 121: 1981–2019. https://doi.org/10.1021/acs.chemrev.0c00977.

[31] Jiang X, Stockwell BR, Conrad M. Ferroptosis: mechanisms, biology and role in disease. Nature Reviews. Molecular Cell Biology. 2021; 22: 266–282. https://doi.org/10.1038/s41580-020-00324-8.

[32] Xie Y, Hou W, Song X, Yu Y, Huang J, Sun X, *et al*. Ferroptosis: process and function. Cell Death and Differentiation. 2016; 23: 369–379. https://doi.org/10.1038/cdd.2015.158.

[33] Kong N, Chen X, Feng J, Duan T, Liu S, Sun X, *et al*. Baicalin induces ferroptosis in bladder cancer cells by downregulating FTH1. Acta Pharmaceutica Sinica. B. 2021; 11: 4045–4054. https://doi.org/10.1016/j.apsb.2021.03.036.

[34] Brigelius-Flohé R, Maiorino M. Glutathione peroxidases. Biochimica et Biophysica Acta. 2013; 1830: 3289–3303. https://doi.org/10.1016/j.bbagen.2012.11.020.

[35] Lei P, Bai T, Sun Y. Mechanisms of Ferroptosis and Relations With Regulated Cell Death: A Review. Frontiers in Physiology. 2019; 10: 139. https://doi.org/10.3389/fphys.2019.00139.

[36] Dietrich C, Hofmann TG. Ferroptosis Meets Cell-Cell Contacts. Cells. 2021; 10: 2462. https://doi.org/10.3390/cells10092462.

[37] Yang WS, SriRamaratnam R, Welsch ME, Shimada K, Skouta R, Viswanathan VS, *et al*. Regulation of ferroptotic cancer cell death by GPX4. Cell. 2014; 156: 317–331. https://doi.org/10.1016/j.cell.2013.12.010.

[38] Proneth B, Conrad M. Ferroptosis and necroinflammation, a yet poorly explored link. Cell Death and Differentiation. 2019; 26: 14–24. https://doi.org/10.1038/s41418-018-0173-9.

[39] Dixon SJ, Patel DN, Welsch M, Skouta R, Lee ED, Hayano M, *et al*. Pharmacological inhibition of cystine-glutamate exchange induces endoplasmic reticulum stress and ferroptosis. eLife. 2014; 3: e02523. https://doi.org/10.7554/eLife.02523.

[40] Fan Z, Wirth AK, Chen D, Wruck CJ, Rauh M, Buchfelder M, *et al*. Nrf2-Keap1 pathway promotes cell proliferation and diminishes ferroptosis. Oncogenesis. 2017; 6: e371. https://doi.org/10.1038/oncsis.2017.65.

[41] Feng L, Zhao K, Sun L, Yin X, Zhang J, Liu C, *et al*. SLC7A11 regulated by NRF2 modulates esophageal squamous cell carcinoma radiosensitivity by inhibiting ferroptosis. Journal of Translational Medicine. 2021; 19: 367. https://doi.org/10.1186/s12967-021-03042-7.

[42] Yan R, Xie E, Li Y, Li J, Zhang Y, Chi X, *et al*. The structure of erastin-bound xCT-4F2hc complex reveals molecular mechanisms underlying erastin-induced ferroptosis. Cell Research. 2022; 32: 687–690. https://doi.org/10.1038/s41422-022-00642-w.

[43] Tang C, Han JQ, Chen D, Zong S, Liu J, Kan J, *et al*. Recent advances on the biological activities of purple sweet potato anthocyanins. Food Bioscience. 2023; 53: 102670. https://doi.org/10.1016/j.fbio.2023.102670.